

Band Structure and Topological Properties of Graphene in a Superlattice Spin Exchange Field.

Luis Brey*

Instituto de Ciencia de Materiales de Madrid, CSIC, 28049 Cantoblanco, Spain

A.R.Carvalho

Instituto de Física, Universidade Federal Fluminense, 24210-346 Niterói, RJ, Brazil

H.A.Fertig

Department of Physics, Indiana University, Bloomington, Indiana 47405, USA

(Dated: May 28, 2022)

We analyze the energy spectrum of graphene in the presence of spin-orbit coupling and a unidirectionally periodic Zeeman field, focusing on the stability and location of Dirac points it may support. It is found that the Dirac points at the K and K' points are generically moved to other locations in the Brillouin zone, but that they remain present when the Zeeman field $\vec{\Delta}(x)$ integrates to zero within a unit cell. A large variety of locations for the Dirac points is shown to be possible: when $\vec{\Delta} \parallel \hat{z}$ they are shifted from their original locations along the direction perpendicular to the superlattice axis, while realizations of $\vec{\Delta}(x)$ that rotate periodically move the Dirac points to locations that can reflect the orbit of the rotating electron spin as it moves through a unit cell. When a uniform Zeeman field is applied in addition to a periodic $\vec{\Delta} \parallel \hat{z}$ integrating to zero, the system can be brought into a metallic, Dirac semimetal, or insulating state, depending on the direction of the uniform field. The latter is shown to be an anomalous quantum Hall insulator.

I. INTRODUCTION

Many of the the proposed technological applications of graphene rely on the possibility of opening gaps at the Dirac points in its band structure [1, 2]. Such gaps would also allow the experimental study of remarkable exotic physical effects that have been predicted by theory [3, 4]. The interest in this system increases greatly if in addition to the band gap, the resulting band structure supports non-trivial topology [5, 6]. Because of the high mobility of its carriers, graphene potentially could be an ideal system for studying electronic properties of a system with momentum-space Berry's curvature [7].

Different strategies have been proposed to endow graphene with topological character. One approach involves the commensurate stacking of graphene on hexagonal boron nitride [8–10]. Another strategy is to induce spin-orbit coupling in the system and thereby open gaps in the spectrum. Along these lines, it has been proposed that a combination of an exchange field and Rashba spin-orbit coupling (SOC) will open such gaps at the Dirac points in monolayer [11–13] and bilayer [14, 15] graphene. This gapped phase is a realization of the quantum anomalous Hall (QAH) insulator in graphene, with a non-vanishing Chern number and accompanying gapless edge states [11]. The two ingredients for the QAH phase can be provided by Fe adatoms [11] or by adsorption of randomly distributed heavy adatoms in the presence of a proximity-induced exchange field [16]. Coupling between graphene and an antiferromagnetic insulator also could

induce the anomalous quantum Hall phase [17].

In this work we discuss the effects of a unidirectional superlattice Zeeman field on the electronic and topological properties of graphene. This could be induced by spin-exchange with an appropriate substrate, an external magnetic field, or some combination of the two. When spin is a good quantum number, this is equivalent for each spin species to a unidirectional periodic electrostatic potential, which can induce new Dirac points in graphene [18–22]. In what follows we investigate how this behavior is modified by Rashba spin-orbit coupling (SOC), quantified by an energy scale λ^R . Our analysis, which works in the continuum limit and ignores intervalley scattering, yields results which are essentially the same for states near the K and K' points, so we will explicitly discuss results for the first of these. We have checked with microscopic tight-binding calculations the accuracy of this approximation.

In the absence of SOC, if the exchange potential induces an effective Zeeman field purely in the $\pm\hat{z}$ direction, $\Delta_z(x)$, for each spin there is an effective periodic potential, which throughout this paper we assume varies in the \hat{x} direction. We mostly focus on situations in which the net exchange field, $\int dx \Delta_z(x) = 0$. For weak and/or short wavelength potentials, the main effect of this is to render the dispersion around the Dirac points associated with each spin anisotropic [23]. We find that SOC splits these spin degenerate Dirac cones, pushing their zero energy points away from the K point, onto the k_y axis. For stronger or longer wavelength $\Delta_z(x)$, at zero Rashba SOC, new Dirac points are already present on the k_y axis [18, 19]. We find that with increasing λ^R these higher order Dirac points become gapped, except for narrow ranges of λ^R where the different species of

* Electronic address: brey@icmm.csic.es

Dirac points may be made to approach one another. For most values of λ^R , however, only two Dirac points remain, residing symmetrically along the k_y axis on either side of the K point. In these situations, an application of a uniform Zeeman field, or an imbalance in the positive and negative regions of Δ_z induces gaps in these last two Dirac points, and the band becomes topological, supporting an QAH effect.

We also consider the effects of in-plane Zeeman fields Δ_x and Δ_y . These can arise if an in-plane magnetic field is applied in addition to exchange coupling to a magnetized system. They can also be present if the magnetized substrate contains a one-dimensional array of oppositely oriented domains. Regions between these regions are domain walls, and these generically contain in-plane fields in the \hat{x} direction (Bloch walls) or \hat{y} direction (Néel walls). We shall see that the effect on the energy level structure depends on which of these two cases is realized, and also on whether neighboring domain walls are aligned or anti-aligned. In some cases there is no qualitative effect on the energy dispersion, in others the Dirac points may be moved into the $k_x - k_y$ plane, and in still others they may reside on the \vec{k} axis along the superlattice direction rather than perpendicular to it. An interesting aspect of in-plane Zeeman fields induced by domain walls is that the locations of their zero energy states reflect the closed loop an electron spin traces on the Bloch sphere when it traverses a single period of the superlattice.

Because the carbon atoms are very light, in pristine graphene the SOC is extremely small [24–26]. Recent studies have shown that Rashba SOC is enhanced when graphene is bent with respect to its planar geometry [27, 28]. A combination of this enhanced SOC and a modulated exchange field could allow the realization of configurations presented in this work. Several other approaches could produce a modulation of the effective Zeeman field. The first involves “Origami structures” [29], in which graphene sheets are periodically folded so that the effective magnetic field oscillates in sign as one moves through the graphene layer. A second possibility is to consider carbon nanotubes in contact with an insulating ferromagnet [30]. In these cases, curvature in the graphene sheet enhances λ^R . In a third approach, one may consider a graphene layer placed in close proximity to a ferromagnet with oppositely oriented magnetic domains alternating along some direction. Finally, an exchange field coupling to the electron spin may be created by depositing hydrogen atoms on the graphene surface [31–33].

This article is generally divided into two parts. In the first we describe our analysis of the system when the exchange field is purely along the \hat{z} direction. We present a perturbative analysis of the system, as well as tight-binding study results. Finally we present a non-perturbative analysis (with details in an appendix) that both confirms the perturbative results, and shows what happens to the higher order Dirac points present in the absence of SOC. In the second part, we discuss the ef-

fects of additional field components in the $\hat{x} - \hat{y}$ plane. We begin with a perturbative analysis of uniform in-plane fields. We then present analyses of two models that include domain walls, one using a uniformly rotating exchange field, and the other a piecewise-constant exchange field. This is followed by a discussion of numerical tight-binding studies. We finally conclude with a discussion and summary.

II. UNIDIRECTIONAL ZEEMAN FIELDS

We begin by considering models in which the effective Zeeman field is always aligned in the \hat{z} direction. The Hamiltonian for such systems consist of three terms,

$$H = H_0 + H_R + H_\Delta, \quad (1)$$

with H_0 the kinetic energy, H_R the Rashba SOC, and H_Δ is a spin-orienting term. In the absence of SOC, the conduction and valence bands touch to form Dirac points at the K and K' points in the Brillouin zone. Near these points the low energy physics is described by the Hamiltonian

$$H_0 = \hbar v_F (-is\sigma_0 \otimes \tau_x \partial_x - i\sigma_0 \otimes \tau_y \partial_y), \quad (2)$$

where v_F is the Fermi velocity of the electrons, $s = 1$ ($s = -1$) for the K (K') valley, and $\vec{\tau}$ is a vector of Pauli matrices acting on a spinor specifying the amplitudes of the wavefunction on the A and B sublattices of graphene. A second vector of Pauli matrices $\vec{\sigma}$ acts on the real spin degree of freedom of an electron, and accompanying both the $\vec{\tau}$ and $\vec{\sigma}$ matrices are corresponding unit matrices, τ_0 and σ_0 .

Rashba SOC appears because of broken mirror symmetry, by interaction with a substrate or induced by heavy adatoms [16]. In the continuum approximation the SOC Rashba term takes the form [34],

$$H_{SO}^R = \frac{1}{2} \lambda^R (-\sigma_x \otimes \tau_y + s \sigma_y \otimes \tau_x). \quad (3)$$

Finally we include a unidirectional superlattice effective Zeeman field, which contributes to the Hamiltonian via

$$H_\Delta = \Delta_z(x) \sigma_z \otimes \tau_0. \quad (4)$$

For this section we consider an antiperiodic exchange term, i.e., $\Delta_z(x + L/2) = -\Delta_z(x)$, where L is the period of the Zeeman field.

As noted in the Introduction, the analytic Hamiltonians we consider in this work are continuum approximations which are appropriate when intervalley scattering is negligible. In general this occurs when the Zeeman field varies over length scales which are large compared to the graphene lattice parameter. Adopting this assumption, in the rest of this paper we will explicitly discuss results only for the K valley ($s = 1$). Within this assumption, results for the K' valley are essentially identical.

A. Symmetry Considerations

In what follows we will be mostly interested in the energy spectrum of this system as a function of \vec{k} , the deviation of the momentum from the Dirac point. It is helpful to begin by considering some symmetries of the system. One of these is a chiral symmetry operation [35] T , consisting of a combined operation of a sublattice chiral operator, $\sigma_0 \otimes \tau_z$, and a shift operator $x \rightarrow x + L/2$, so that

$$T^\dagger H(x) T = (\sigma_0 \otimes \tau_z) H(x + \frac{L}{2}) (\sigma_0 \otimes \tau_z) = -H(x). \quad (5)$$

Because T commutes with the translation operator, it preserves wavevector, so the anticommutation property of T with H guarantees that for any state at wavevector \vec{k} of energy $\epsilon(\vec{k})$, there is a corresponding state at the same wavevector with energy $-\epsilon(\vec{k})$.

A second observation is that, because the Hamiltonian does not depend on y , the momentum in the y direction, k_y , is a good quantum number. Writing a wavefunction in the form $\vec{\Phi}_{k_x, k_y}(x, y) = e^{ik_y y} \vec{\Psi}(x)$, the effective Hamiltonian acting on $\vec{\Psi}$ becomes $H(k_y) \equiv e^{-ik_y y} H e^{ik_y y}$, and has the property

$$H(-k_y) = \sigma_z \otimes \tau_0 H^*(k_y) \sigma_z \otimes \tau_0. \quad (6)$$

This implies that for any zero mode of Eq. 1 appearing at

a particular value of $k_y \equiv k_y^*$, we can construct another zero mode with $k_y = -k_y^*$.

Finally, the Hamiltonian commutes with a generalized mirror operator $X = \sigma_x \otimes \tau_y I_x$, where $I_x f(x) = f(-x)$, and assuming $\Delta(-x) = -\Delta(x)$, one may easily show $[X, H] = 0$. Moreover, X satisfies $\{T, X\} = 0$ and $X^2 = 1$. This means that states which are chiral partners (in general with energies E and $-E$) have opposite eigenvalues of the operator X . This allows the system to support Dirac points; i.e., when $\epsilon(\vec{k})$ approaches 0 as \vec{k} is varied, it is not repelled by its chiral partner with which it becomes degenerate. The X operator can be exploited to help locate zero modes for this system, as we show below.

B. Perturbation Theory

When the spin-orbit coupling is zero ($\lambda^R = 0$), the Hamiltonian consist of two uncoupled blocks with well-defined spin quantum numbers, each of which supports a zero energy Dirac point at $\vec{k} = 0$ [18, 36]. For small λ^R one can obtain the effective Hamiltonian in the vicinity of this point using degenerate perturbation theory; i.e., by projecting the Hamiltonian onto the zero energy basis for $\lambda^R = 0$. The four zero energy states have the explicit forms

$$\psi_{\uparrow,+} = \frac{1}{\sqrt{L}} \begin{pmatrix} \cos \theta(x) \\ -i \sin \theta(x) \\ 0 \\ 0 \end{pmatrix}, \psi_{\uparrow,-} = \frac{1}{\sqrt{L}} \begin{pmatrix} -i \sin \theta(x) \\ \cos \theta(x) \\ 0 \\ 0 \end{pmatrix}, \psi_{\downarrow,+} = \frac{1}{\sqrt{L}} \begin{pmatrix} 0 \\ 0 \\ \cos \theta(x) \\ i \sin \theta(x) \end{pmatrix}, \psi_{\downarrow,-} = \frac{1}{\sqrt{L}} \begin{pmatrix} 0 \\ 0 \\ i \sin \theta(x) \\ \cos \theta(x) \end{pmatrix}, \quad (7)$$

with

$$\theta(x) = -\frac{1}{\hbar v_F} \int_0^x \Delta(x) dx. \quad (8)$$

Multiplying the states in Eq. 7 by $e^{i\vec{k} \cdot \vec{r}}$, the projected Hamiltonian (Eq.1) in the resulting basis takes the form

$$H = \begin{pmatrix} 0 & \hbar v_F(k_x - ik_y f_0) & 0 & -i \frac{\lambda^R}{2} (1 + f_0) \\ \hbar v_F(k_x + ik_y f_0) & 0 & i \frac{\lambda^R}{2} (1 - f_0) & 0 \\ 0 & -i \frac{\lambda^R}{2} (1 - f_0) & 0 & \hbar v_F(k_x - ik_y f_0) \\ i \frac{\lambda^R}{2} (1 + f_0) & 0 & \hbar v_F(k_x + ik_y f_0) & 0 \end{pmatrix}, \quad (9)$$

with

$$f_0 = \frac{1}{L} \int_0^L \cos 2\theta(x) dx. \quad (10)$$

The effective Hamiltonian Eq. 9 has zero energy solutions. These zero modes appear at momentum \vec{k}^* , with

$$k_x^* = 0, \quad k_y^* = \pm \frac{\lambda^R}{2\hbar v_F f_0} \sqrt{1 - f_0^2}. \quad (11)$$

One may further expand Eq. 9 around \vec{k}^* by projecting it onto the two zero mode states at that point. Diagonal-

izing the resulting 2×2 Hamiltonian yields the dispersion law

$$\epsilon(\tilde{k}_x, \tilde{k}_y) = \hbar v_F \sqrt{1 - f_0^2 \sqrt{k_x^2 + f_0^2 \tilde{k}_y^2}}, \quad (12)$$

where $\tilde{k}_{x,y} = k_{x,y} - k_{x,y}^*$ is the momentum measured relatively to the Dirac points, Eq. 11.

C. Tight Binding Studies

The band structure of pristine graphene is well-described by a tight-binding model with hopping $t \sim 2.7\text{eV}$ between nearest neighbor atoms on a honeycomb lattice, represented by

$$H_0 = -t \sum_{\langle i,j \rangle, \sigma} c_{i,\sigma}^\dagger c_{j,\sigma} \quad (13)$$

where $c_{i,\sigma}^\dagger$ creates an electron at site i with spin σ . Rashba SOC in this system can be implemented as a spin-dependent hopping between nearest neighbors of the form

$$H_R = i \frac{\lambda^R}{3} \sum_{\langle i,j \rangle} \sum_{s,s'} \hat{z} \cdot (\vec{\sigma} \times \hat{u}_{ij})_{s,s'} c_{i,s}^\dagger c_{j,s'}, \quad (14)$$

where \hat{u}_{ij} is a unit vector pointing from site j to site i and $\vec{\sigma}$ is the vector of spin Pauli matrices. Finally the Zeeman coupling is implemented through a term of the form

$$H_\Delta = \sum_{i,s,s'} \Delta(i) c_{i,s}^\dagger (\sigma_z)_{s,s'} c_{i,s'} \quad (15)$$

where $\Delta(i)$ is the periodic Zeeman field.

For simplicity we consider here a Kronig-Penney model Zeeman field. Writing this in the form $\Delta(x) = \Delta_0 \text{sgn}(x)$ for $|x| < L/2$, one finds for the expressions in the last subsection [20, 21],

$$f_0 = \frac{|\sin u|}{u} \quad \text{with} \quad u = \frac{\Delta_0 L}{2\hbar v_F}. \quad (16)$$

A typical band dispersion obtained from diagonalizing the tight-binding Hamiltonian is illustrated in the inset of Fig. 1(a). For $\lambda^R = 0$ one obtains two degenerate Dirac cones centered at the K point. As expected from our perturbative analysis, for $\lambda^R \neq 0$ these are repelled down the k_y axis, settling at values $k_y = \pm k_y^*$ that depend on λ^R , L , and Δ_0 . In Fig. 1(a) and (b) we plot the dependence of k_y^* on the Rashba and exchange field respectively, as obtained from the tight-binding calculation and from Eqs. 11 and 16. The agreement between the tight-binding calculations and our perturbative analysis is very good when the parameter $u = \frac{\Delta_0 L}{2\hbar v_F}$ is smaller than π . For larger values, new Dirac points emerge in the spectrum of the decoupled spin Hamiltonians [18, 36]. The projected Hamiltonian (in the states described by Eq. 7)

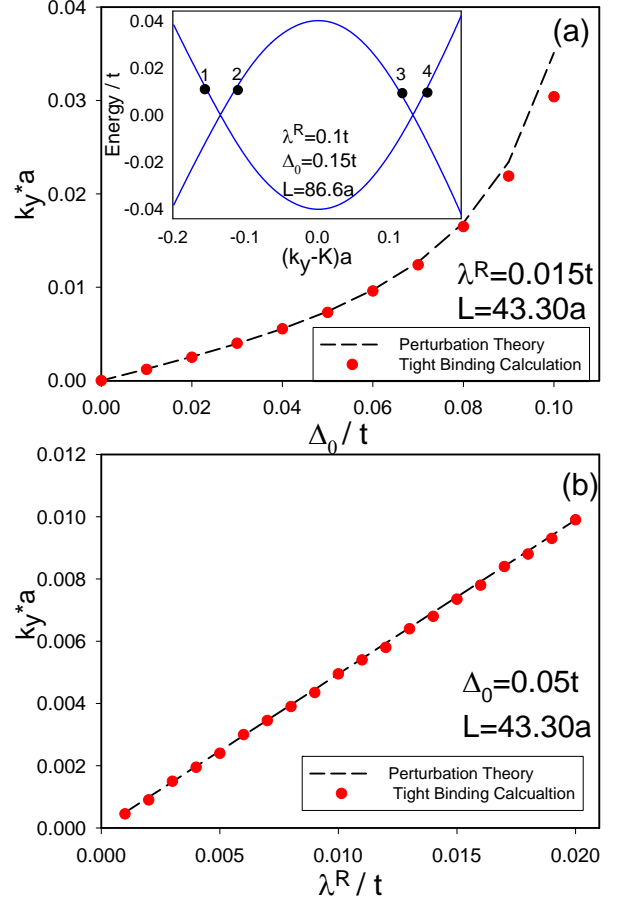


FIG. 1. (Color online) (a) and (b) position of the split Dirac points as a function of the intensity of the periodic exchange field and Rashba SOC respectively. Red dots indicate the tight binding results, whereas the lines are continuum results obtained from Eq. 11 and Eq. 16. In the inset of (a) we plot a typical tight binding band structure near the original Dirac point. The quantity a is the graphene lattice parameter.

is not sufficient to capture this physics. Not surprisingly, as this regime is approached the predictions of Section IIB become inaccurate. Below we discuss the behavior of the higher-order Dirac points associated with large u when $\lambda^R \neq 0$.

D. Edge State Interpretation, Reflection Symmetry, and Quantized Transport

Some insight about the nature of the SOC-split Dirac points is obtained by examining wave functions of states near zero energy. In Fig. 2 we plot the absolute square of the wave functions corresponding to the four states marked in the inset of Fig. 1. Interestingly, the states are largely localized at the (two) interfaces of the unit cell separating regions of opposite signed Zeeman fields. Moreover, the direction of the group velocity associated with these states correlates with the sign of the Zeeman

field steps around which they are located: up-steps and down-steps support states of opposite velocity. Notice that for a given energy there are *two* such states at a given interface in the vicinity of the K point. Two further states for each interface can be found near the K' point.

These interface states are similar to those appearing in bilayer graphene in an electrostatic lateral confinement step [37, 38], and in periodically modulated bilayer graphene [39–41]. The origin of these interface states is topological. Graphene in the presence of Rashba SOC and constant exchange coupling Δ is a quantum anomalous Hall system [11] with Hall conductivity

$$\sigma_{xy} = \frac{e^2}{h} C, \quad (17)$$

where $C=2\text{sgn}(\Delta)$ is the Chern number associated with the full band, and the factor of 2 enters due to the two Dirac points (valleys) in graphene. Because of the different Chern numbers in each region, at their interface there should appear four parallel velocity edge channels. For a generic superlattice of such interfaces, their coupling will generally gap out the spectrum; however, in the presence of an appropriate reflection symmetry (specifically the X operator above), for certain choices of $\vec{k} \equiv \vec{k}^*$ there are zero energy states [40]. This is the origin of the two Dirac points per valley that appear at this superlattice.

The above discussion emphasizes the role of reflection symmetry in the form of the operator X in leading to a gapless spectrum. By contrast if this symmetry is broken one might expect a gap to open [40]. Moreover, since the system is not time-reversal symmetric, non-zero quantized Hall transport may result. The simplest perturbation one can introduce that does this is an overall magnetic field in the \hat{z} -direction coupling to the spins, which may be a result of an imbalance between the two directions of the exchange field, or simply from an applied magnetic field weak enough that the coupling to orbital motion may be ignored. To the Hamiltonian in Eq. 9 this adds a term of the form

$$\Delta H = \begin{pmatrix} b_z & 0 & 0 & 0 \\ 0 & b_z & 0 & 0 \\ 0 & 0 & -b_z & 0 \\ 0 & 0 & 0 & -b_z \end{pmatrix}. \quad (18)$$

One can show this indeed opens a gap by examining the Hamiltonian $H + \Delta H$ when it is projected into the subspace of zero energy states of H (Eq. 9). Defining Pauli matrices μ for which $\mu_x|\psi_{\sigma,\pm}\rangle = \pm|\psi_{\sigma,\pm}\rangle$, where $\sigma = \uparrow, \downarrow$ denotes spin, and $|\psi_{\sigma,\pm}\rangle$ are the kets corresponding to Eqs. 7, linear combinations may easily be constructed such that $\mu_z|\mu_z = \pm, \sigma\rangle = \pm|\mu_z = \pm, \sigma\rangle$. In terms of these one finds, for example at $\vec{k}^* = (0, k_y^*)$, two zero

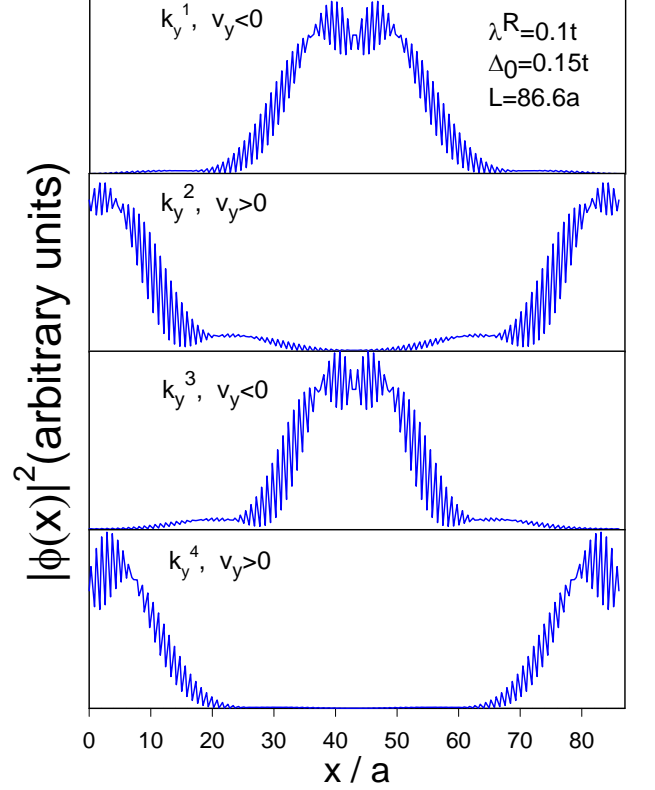


FIG. 2. (Color online) Square of the wave function as function of the position, of the four states, 1-4, marked in the inset of Fig.1(a), v_y indicates the velocity of the states along the \hat{y} -direction. a is the graphene lattice parameter.

modes which can be labeled by μ_z ,

$$\begin{aligned} |1\rangle_{k^*} &\equiv \frac{\sqrt{1-f_0}}{\sqrt{2}}|\mu_z = 1, \uparrow\rangle + \frac{\sqrt{1+f_0}}{\sqrt{2}}|\mu_z = 1, \downarrow\rangle, \\ |-1\rangle_{k^*} &\equiv \frac{\sqrt{1+f_0}}{\sqrt{2}}|\mu_z = -1, \uparrow\rangle + \frac{\sqrt{1-f_0}}{\sqrt{2}}|\mu_z = -1, \downarrow\rangle. \end{aligned} \quad (19)$$

Projection of $H + \Delta H$ into the $(|1\rangle_{k^*}, |-1\rangle_{k^*})$ basis yields an effective Hamiltonian H_{k^*} given by

$$H_{k^*} = v_F \sqrt{1-f_0^2} \begin{pmatrix} b_z \frac{f_0}{\sqrt{1-f_0^2}} & \tilde{k}_x - i f_0 \tilde{k}_y \\ k_x + i f_0 \tilde{k}_y & -b_z \frac{f_0}{\sqrt{1-f_0^2}} \end{pmatrix},$$

where $\tilde{k} = \vec{k} - \vec{k}^*$. The energy eigenvalues are

$$\varepsilon(\tilde{k}_x, \tilde{k}_y) = \pm \sqrt{v_f^2(1-f_0^2)(\tilde{k}_x^2 + f_0 \tilde{k}_y^2) + (f_0 b_z)^2},$$

which is in general gapped, as expected. Clearly one may use the basis in Eq. 19 to examine the effects of Zeeman fields in the \hat{x} and \hat{y} directions as well; however we defer this discussion to the next section.

Qualitatively, the gap opening is associated with a net effective Zeeman field which is predominantly up or down in the \hat{z} direction, so one may expect that the Chern number associated with the resulting positive or negative energy band closest to zero energy will be the same as for the corresponding system with a uniform Zeeman field. We have confirmed that this is indeed true. In Fig. 3 we plot numerically obtained energy levels near the K point, in the presence of Rashba SOC, a piecewise-constant periodic exchange field, and a constant Zeeman field Δ_c . For any finite Δ_c we find the spectrum is gapped. Similar physics applies if the unit cell is asymmetric. Fig. 4 illustrates numerical results for energy levels in such a case, where the periodic exchange field has larger regions of positive exchange field than negative exchange field; i.e., $L_+/L_- > 1$. Again the spectrum is gapped.

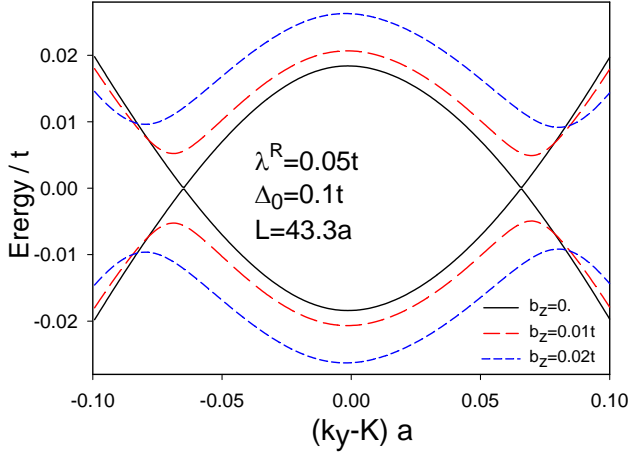


FIG. 3. (Color online) Tight-binding band structure near the Dirac point K obtained with the parameters $\lambda^R=0.05t$, $\Delta_0=0.1t$, $L=43.3a$ and different values of an overall exchange field pointing in the z -direction, b_z .

With such numerical tight-binding results we can compute the Hall conductivity associated with a band, which is a direct measure of its Chern number. Specifically,

$$\sigma_{xy} = -2 \frac{e^2 \hbar}{S} \sum_{n,n',\mathbf{k}} \frac{\text{Im}(\langle n\mathbf{k}|v_x|n'\mathbf{k}\rangle \langle n'\mathbf{k}|v_y|n\mathbf{k}\rangle)}{(\varepsilon_{n,\mathbf{k}} - \varepsilon_{n',\mathbf{k}})^2}, \quad (20)$$

where S is the sample area and the velocity operator is given by

$$\mathbf{v} = -\frac{i}{\hbar} t \sum_{\langle i,j \rangle, \sigma} (\mathbf{r}_i - \mathbf{r}_j) c_{i,\sigma}^\dagger c_{j,\sigma}, \quad (21)$$

At present we are interested in the spectrum of Eq. 1 when there is antisymmetry in the exchange field,

with \mathbf{r}_i the position of carbon atom at site i . For both cases described above one finds within numerical error that

$$\sigma_{xy} = 2 \frac{e^2}{h} \text{sgn}(\bar{\Delta}), \quad (22)$$

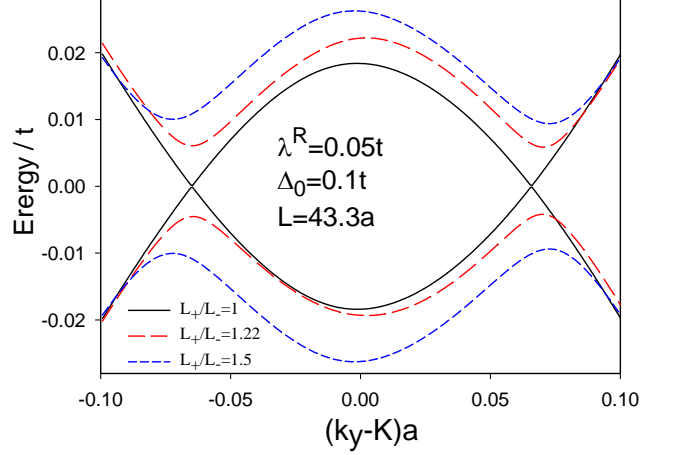


FIG. 4. (Color online) Tight-binding band structure near the Dirac point K obtained with the parameters $\lambda^R=0.05t$, $\Delta_0=0.1t$, $L=43.3a$ and different values of the ratio L_+/L_- , see text.

where $\bar{\Delta}$ is the average value of the effective Zeeman field, including the contribution from Δ_c . Thus these systems support a quantum anomalous Hall effect, in which there is quantized Hall transport even in the absence of an orbital magnetic field affecting the electron dynamics.

E. Zero Modes Beyond Perturbation Theory

We finish this section with a non-perturbative analysis of zero modes. To this point we have focused on zero modes which are located at the K and K' points for $\lambda^R = 0$, and which split and move out the k_y axis when SOC is turned on. In the absence of SOC, however, for sufficiently large $|\Delta_z|L$ there will be further Dirac points for each spin on the k_y axis [18, 19]. We would like to understand how these evolve with λ^R .

$\Delta_z(-x) = -\Delta_z(x)$. Eigenstates in such cases may be

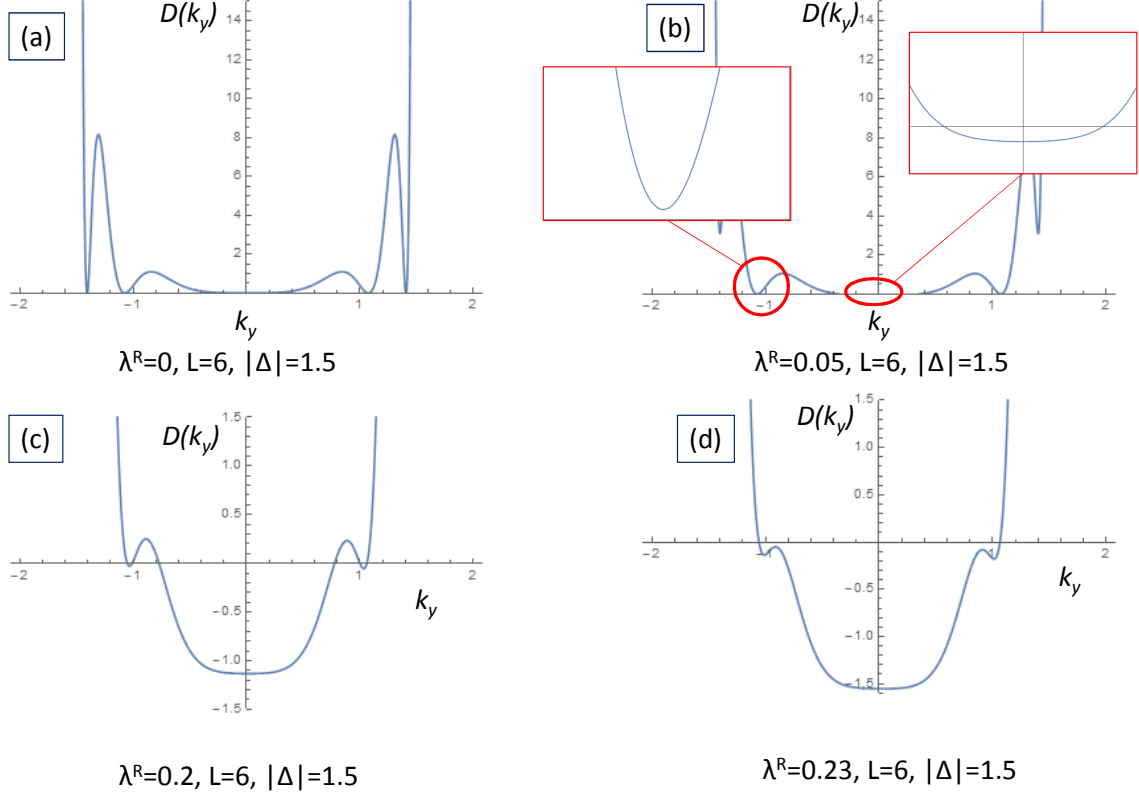


FIG. 5. (Color online) Plots of the function $D(k_y)$, which vanishes at values of k_y where there are zero energy states on the k_y axis. (a) $\lambda^R = 0$, illustrating Dirac points at $k_y = 0$ as well as at non-vanishing values of k_y . (b) $\lambda^R = 0.05$. Insets show that higher order vanishings of $D(k_y)$ are lifted off the k_y axis so that these Dirac points are eliminated, while the degenerate Dirac points at $k_y = 0$ are repelled down the k_y axis but are not eliminated. (c) $\lambda^R = 0.20$ and (d) $\lambda^R = 0.23$ illustrate that multiple Dirac points can emerge over narrow ranges of λ^R at non-vanishing k_y . For all panels, unit cell length is $L = 6a$ and $|\Delta| = 1.5\hbar v_F/a$. All λ^R values are in units of $\hbar v_F/a$.

characterized by a quantum number associated with the reflection operator X . Using a transfer matrix approach one may express the condition that a zero mode exists for a given value of k_y as being met if the determinant a particular 2×2 real matrix $D(k_y)$ vanishes. The demonstration of this is somewhat involved; details are provided in the Appendix. Fig. 5 illustrates a typical evolution of $D(k_y)$ as λ^R is raised from zero. Exactly at $\lambda^R = 0$ there are several zeros, reflecting the multiple Dirac points expected for this situation [18]. It should be noted there are

two degenerate Dirac cones around each of these points, one for each value of spin which is a good quantum number in this situation. When λ^R is first raised from zero, these admix and repel, leading to gaps everywhere except near $k_y = 0$, where the degenerate Dirac points at the origin are split into two and move down the k_y axis. With increasing λ^R these migrate further from the K point, and may interact with residual structure from the higher order Dirac points to produce extra Dirac points over narrow ranges, as illustrated in Fig. 5(c). With the

exception of these situations, however, we find that only the two Dirac points predicted by the perturbative analysis are stable when SOC is present. Finally, we note that this analysis verifies that corrections at higher orders in perturbation theory do not open gaps at these Dirac points.

III. IN-PLANE EXCHANGE AND ZEEMAN FIELDS

In this section we explore what happens to the spectrum when the effective Zeeman field is not strictly oriented in the $\pm\hat{z}$ direction. There are two reasons for considering such situations. Firstly, in addition to a periodic field induced by interaction with a substrate, one may introduce a uniform external magnetic field with an arbitrary size and orientation. Such situations are interesting because, as we shall see, the spectrum is relatively sensitive to these, so that one may in principle significantly modify the electronic structure in a single system just by modifying the external field. A second class of systems in which in-plane Zeeman fields may be relevant are those in which electrons in the graphene sheet are coupled to a system with magnetic domains with equal and opposite orientations. Such magnetic domain structures are common in many ferromagnets, but the regions separating domains are rarely sharp, and often support domain walls in which the magnetization rotates continuously between opposing directions of the magnetization. Thus the electrons encounter localized regions of in-plane field. Similarly, a periodic Zeeman field can in principle be implemented by subjecting a folded stack of graphene to an external magnetic field (which we presume to be sufficiently weak that orbital effects of the field can be ignored.) In this case the Zeeman field effectively rotates in the folded sections of the stack, and once again localized regions of in-plane field will be present.

We begin by examining the simplest of these cases, a uniform Zeeman field present in addition to the periodic $\Delta_z(x)$ field.

A. Uniform In-Plane Zeeman Fields

The impact of an externally imposed uniform Zeeman field on the Dirac points near the K point can be easily assessed perturbatively, using the states appearing in Eq. 19 in the same way as for H_{k^*} (Eq. 20) to assess the effect of a uniform field in the \hat{z} direction. Following the same procedure we find, for a perturbation of the form $\Delta H_Z = \vec{b} \cdot \vec{\sigma}$,

$$H_{k^*}(\mathbf{b}) = v_F \sqrt{1 - f_0^2} \begin{pmatrix} b_x + b_z \frac{f_0}{\sqrt{1-f_0^2}} & \tilde{k}_x - i f_0 \tilde{k}_y \\ k_x + i f_0 \tilde{k}_y & b_x - b_z \frac{f_0}{\sqrt{1-f_0^2}} \end{pmatrix}.$$

One can see that, as noted before, the b_z contribution opens gaps at the Dirac points, while b_y has no qualita-

tive effect on the spectrum, and b_x shifts the Dirac point away from zero energy. For the last of these, the same analysis shows that b_x component shifts the Dirac point at $k_y = -k^*$ in the opposite direction energetically, so that b_x by itself creates both electron-like and hole-like Fermi surfaces when the graphene is undoped, enhancing the conductivity of the system. The choice of orientation of \vec{b} in the $\hat{x} - \hat{z}$ plane thus allows one to tune the system between an insulator and a metal. Finally, at this level of approximation it is interesting to note that b_y has no effect on the spectrum.

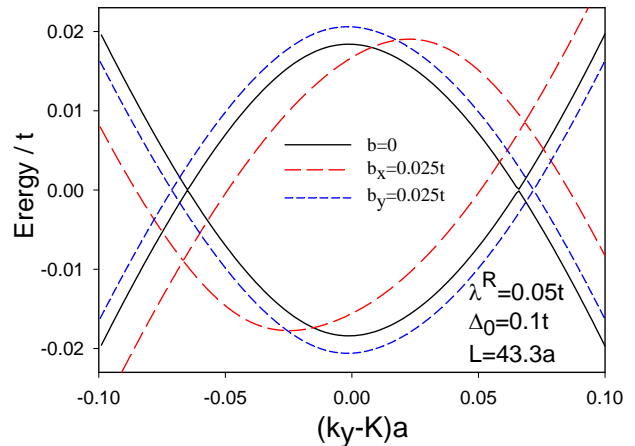


FIG. 6. (Color online) Tight-binding band structure near the Dirac point K obtained with the parameters $\lambda^R=0.05t$, $\Delta_0=0.1t$, $L=43.3a$ and overall exchange fields pointing in the x and y directions.

Numerical tight-binding calculations support these results. Fig. 6 illustrates both the upward/downward energetic shifts of the Dirac points with b_x and the gap opening with b_z occur as expected. Moreover, the stability of the Dirac points at zero energy with respect to b_y is confirmed, although they move slightly in their location on the k_y axis. This behavior presumably occurs due to corrections above linear order in b_y which our perturbative analysis does not capture. We will see that analogous motion of zero modes is induced by domain wall structures.

B. Uniformly Rotating Zeeman Field

As a simple model of a Zeeman field that rotates into different directions, we consider one that rotates uniformly around either the \hat{y} or the \hat{x} directions. Explicitly,

$$\begin{aligned} \Delta_z &= \Delta_0 \sin \alpha(x), \\ \Delta_x &= \Delta_0 \cos \alpha(x) \cos \chi, \\ \Delta_y &= \Delta_0 \cos \alpha(x) \sin \chi, \end{aligned} \quad (23)$$

with $\alpha(x)=Gx$. To analyze this model we form a basis by diagonalizing the Hamiltonian $H_0 + \Delta_z(x)\sigma_z$ precisely as

in Section II B, yielding four zero energy states at the K point. Expanding the full Hamiltonian $H_0 + \vec{\Delta}(x) \cdot \vec{\sigma} + H_R$

in these states (multiplied by plane waves $e^{i\vec{k} \cdot \vec{r}}$) yields a 4×4 Hamiltonian

$$H = \begin{pmatrix} 0 & \hbar v_F(k_x - ik_y f_0) & 0 & -i\frac{\lambda_R}{2}(1 + f_0) + \Delta_0 f_1 e^{i\chi} \\ \hbar v_F(k_x + ik_y f_0) & 0 & i\frac{\lambda_R}{2}(1 - f_0) + \Delta_0 f_1 e^{i\chi} & 0 \\ 0 & -i\frac{\lambda_R}{2}(1 - f_0) + \Delta_0 f_1 e^{-i\chi} & 0 & \hbar v_F(k_x - ik_y f_0) \\ i\frac{\lambda_R}{2}(1 + f_0) + \Delta_0 f_1 e^{-i\chi} & 0 & \hbar v_F(k_x + ik_y f_0) & 0 \end{pmatrix}, \quad (24)$$

where

$$f_1 \equiv \int_{-L/2}^{L/2} dx \cos \alpha(x) \sin 2\theta(x).$$

Using degenerate perturbation theory, we can search for the positions of the zero modes in the k_x, k_y plane. Assuming these to be small, to quadratic order these are given by the solutions to

$$\begin{aligned} \hbar^2 v_F^2 (k_x^2 - f_0 k_y^2) &= \Delta_0^2 f_1^2 - \frac{\lambda_R^2}{4} (1 - f_0^2) + \Delta_0 f_1 \lambda_R f_0 \cos \chi \\ \hbar^2 v_F^2 k_x f_0 k_y &= \Delta_0 f_1 \frac{\lambda_R}{2} \sin \chi. \end{aligned} \quad (25)$$

A first observation is that when $\lambda_R=0$, the zeros are always on the k_x axis, in contrast to the various results we found in the last section. For $\chi = \pi/2$ or $3\pi/2$, where the Zeeman field vector is transverse to superlattice axis – a simple model for Néel domain walls, as we discuss in the next subsection – one finds both k_x and k_y are non-zero when $\lambda_R \neq 0$. This agrees with our analysis of a model with piecewise constant $\vec{\Delta}(x)$ which is non-perturbative in this parameter, discussed below.

The other interesting case is $\sin \chi=0$, for which $\vec{\Delta}(x)$ rotates longitudinally, a simple model of Bloch domain walls (again, discussed below.) Because $\sin \chi=0$, k_x or k_y must vanish and the zero modes are on one of the axes. When $\lambda_R=0$, the zero is on the k_x -axis. For $\cos \chi = -1$, one finds that k_x moves towards the origin with increasing λ_R . For $\cos \chi = 1$, k_x initially moves away from the origin with increasing λ_R , but when this parameter is large enough it also moves towards the origin. In both cases the Dirac points at $\pm k_x$ ultimately merge at the origin at some critical value of λ_R , and then repel back out along the k_y axis as λ_R increases further.

Numerical diagonalization of a tight-binding model with this form of $\vec{\Delta}(x)$ confirm these expectations from Eq. 25, indicating that our perturbative approach yields qualitatively correct results. Typical results are illustrated in Fig. 7. We will see in the next subsection that they are also in agreement with a piecewise constant $\vec{\Delta}(x)$ model, for which one may carry out an analysis that is non-perturbative in all of its components.

C. Piecewise Constant Rotating Exchange Fields: Domain Walls

In this subsection we consider the impact of in-plane fields when they occur between regions of constant exchange field Δ_z , which act like Zeeman fields oriented along the \hat{z} direction. To describe such situations we generalize this coupling to be formally the same as for a rotating Zeeman field, $H_\Delta \rightarrow \vec{\Delta}(x) \cdot \vec{\sigma}$ but in this subsection the rotation is not uniform. The regions between locations where $\vec{\Delta} \parallel \hat{z}$ are essentially domain walls (DW's), which, as mentioned briefly in the previous subsection, may have a variety of forms. Most prominent are Bloch walls (in which $\vec{\Delta}$ rotates through the $\Delta_x - \Delta_z$ plane), and Néel walls (in which $\vec{\Delta}$ rotates through the $\Delta_y - \Delta_z$ plane). Each unit cell must contain two DW's, and an additional degree of freedom in this problem is that the sense of rotation (clockwise or counterclockwise) can be the same or different. In the former case, if the DW's have the same gradient profile in $\vec{\Delta}(x)$, and the oppositely directed regions of constant Δ_z have the same magnitude and width, then the net effective Zeeman field in a unit cell vanishes. As previewed in Section III B the rotation of the effective Zeeman field can have a very interesting impact on where Dirac points reside in the Brillouin zone. When the DW's rotate with opposite senses there is a net in-plane effective Zeeman field. We will see numerically below that this situation is already interesting when $\lambda_R = 0$: the system when undoped is metallic, supporting overlapping Fermi surfaces that are electron- and hole-like. The inclusion of SOC however restores the Dirac points, albeit in different locations depending on whether the $\vec{\Delta}$ rotates through the \hat{x} or \hat{y} direction.

To examine the electronic spectrum of such structures, we adopt a simple model in which $\vec{\Delta}(x)$ is piecewise constant, with four separate regions in a unit cell: two in which $\vec{\Delta} \parallel \hat{z}$, and two in which $\vec{\Delta}(x)$ is in either the \hat{x} or the \hat{y} direction. This geometry is illustrated in Fig. 8. Within the unit cell, $\vec{\Delta}(x)$ changes direction at positions $x = x_i$, with $i = 0, 1, 2, 3, 4$, and the two DW regions have width $x_2 - x_1 = x_4 - x_3 \equiv L_{DW}$. $\vec{\Delta}$ in the two DW regions point in the opposite (same) direction when $p = 1$ ($p = -1$). We assume that the two domains in a unit cell have the same size: $x_1 - x_0 = x_3 - x_2$.

1. States and Matching Conditions

Our strategy will be to construct zero modes for $\lambda^R = 0$, and then add in SOC perturbatively. We express states of the Hamiltonian in terms of states which are locally eigenstates of the exchange field. Writing $\vec{\Delta}(x) \equiv |\Delta(x)|\hat{n}(x)$, these are the states which satisfy

$$\hat{n} \cdot \vec{\sigma} \vec{\chi}_{\hat{n}}^{(\pm)} = \pm \vec{\chi}_{\hat{n}}^{(\pm)}. \quad (26)$$

For $\lambda^R = 0$ we anticipate finding zero energy states at $k_y = 0$ (although these turn out to be Dirac points only for $p = 1$), with wavefunctions $\vec{\psi}(x)$ which are annihilated by

$$H' = v_F(-i\tau_x \partial_x) + \vec{\Delta}(x) \cdot \vec{\sigma}(x), \quad (27)$$

where we have set $\hbar = 1$. It is clear that these zero energy states of H' have τ_x as a good quantum number. Writing $\vec{\psi}(x) = \sum_{s=\pm} u_s(x) \vec{\chi}_{\hat{n}}^{(s)}$, one finds in regions of constant $\hat{n}(x)$ that

$$u_{\pm}(x) = u_{\pm}(x_0) \exp \left\{ \pm i\tau_x \int_{x_0}^x dx' |\vec{\Delta}(x')| \right\}. \quad (28)$$

We next define the set of Pauli matrices $\vec{\mu}$ such that $\mu_z \vec{\chi}_{\hat{n}}^{(s)} = s \vec{\chi}_{\hat{n}}^{(s)}$ for any x ; in this representation the quantization axis rotates with $\hat{n}(x)$. Using these, it is not difficult to derive a matching formula across a jump in the direction of $\hat{n}(x)$ at a point x_0 through an angle $\Delta\theta$ in the plane of the initial and final directions of $\hat{n}(x_0^{\pm} \equiv x_0 + 0^{\pm})$. Specifically,

$$\vec{u}(x_0^+) = e^{-\frac{i}{2}\Delta\theta\mu_y} \vec{u}(x_0^-), \quad (29)$$

where $\vec{u} \equiv (u_+, u_-)^{\dagger}$.

For the regions $x_j < x < x_i$ in which $n(x)$ is constant, the wavefunctions may be written

$$\begin{aligned} u_+(x) &= u_{+,ij}^{(0)} e^{-i\tau_x \theta(x, x_j)} \\ u_-(x) &= u_{-,ij}^{(0)} e^{i\tau_x \theta(x, x_j)}, \end{aligned} \quad (30)$$

where $\theta(x, x_j) = |\vec{\Delta}|(x - x_j)/v_F$. Application of the matching condition Eq. 29 at $x = x_1, x_2, x_3, x_4$ leads to the condition

$$\vec{u}(x = x_4^+) = P_{43} P_{32} P_{21} P_{10} \vec{u}(x = x_0^+) \equiv P \vec{u}(x = x_0^+), \quad (31)$$

with matrices

$$P_{ij} = \frac{1}{\sqrt{2}} \begin{pmatrix} e^{-i\tau_x \theta(x_i, x_j)} & -e^{i\tau_x \theta(x_i, x_j)} \\ e^{-i\tau_x \theta(x_i, x_j)} & e^{i\tau_x \theta(x_i, x_j)} \end{pmatrix} \quad (32)$$

for $(i, j) = (1, 0)$ and $(2, 1)$, and

$$P_{ij} = \frac{1}{\sqrt{2}} \begin{pmatrix} e^{-i\tau_x \theta(x_i, x_j)} & -p e^{i\tau_x \theta(x_i, x_j)} \\ p e^{-i\tau_x \theta(x_i, x_j)} & e^{i\tau_x \theta(x_i, x_j)} \end{pmatrix} \quad (33)$$

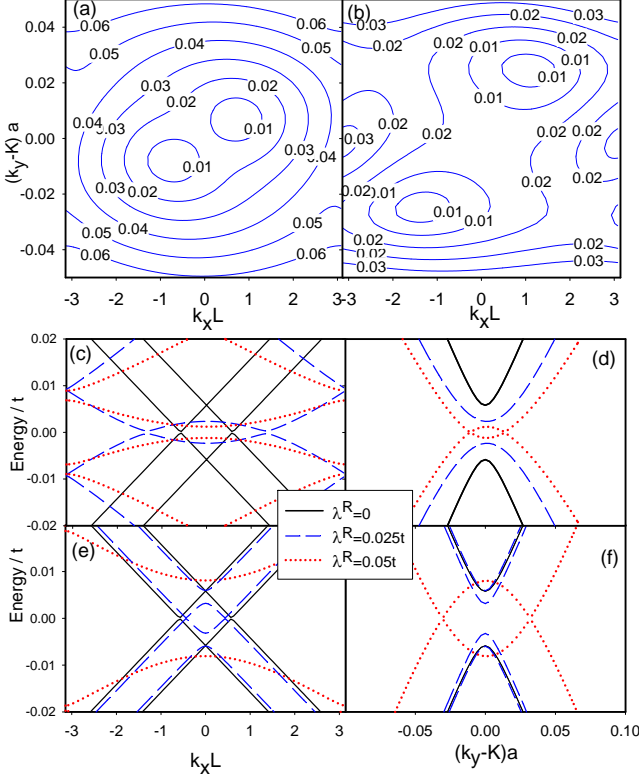


FIG. 7. (Color online) Numerical tight-binding results near the Dirac point K , obtained with the parameters $\Delta_0=0.02t$ and $L=86.6a$, in presence of an uniformly rotating field, Eq. 23. In (a) and (b) we show contour plots of the energy gap for $\chi=\pi/2$ and $\lambda^R=0.005t$ and $\lambda^R=0.028t$ respectively. In this geometry the positions of the Dirac points move in the k_x - k_y plane. In (c)-(d) and (e)-(f) we plot the band structure in the k_x and k_y directions for $\chi=0$ and $\chi=\pi$ respectively, Eq.23.

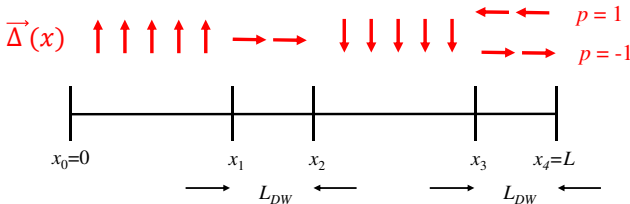


FIG. 8. (Color online) Illustration of the rotation of $\vec{\Delta}$ in the piecewise constant $\vec{\Delta}$ model. For $p = 1$ the domain walls are oriented in opposite directions. For $p = -1$ they are oriented in the same direction.

for $(i, j) = (3, 2)$ and $(4, 3)$, with $p = 1(-1)$ if the DW in $x_3 < x < x_4$ rotates in a clockwise (counterclockwise) sense (see Fig. 8). To obtain a consistent solution, Bloch's theorem requires that P has an eigenvector with eigenvalue $-pe^{ik_x^* L}$, where k_x^* must be real. Using the fact that $\text{Det} P_{ij} = 1$, it is easy to show that the eigenvalues of P have the form $\lambda_{\pm} = \frac{1}{2}[T \pm (T^2 - 4)^{1/2}]$, where T is the trace of P . For the model illustrated in Fig. 8, in which $\theta(x_1, x_0) = \theta(x_2, x_1) \equiv \theta_{10}$ and $\theta(x_2, x_1) = \theta(x_4, x_3) \equiv \theta_{21}$, with some algebra one finds

$$T = -2 [\cos 2\theta_{10} \sin^2 \theta_{21} + p \cos^2 \theta_{21}]. \quad (34)$$

For either sign of p it is easy to see $|T| \leq 2$, so that $|\lambda_{\pm}| = 1$ and k_x^* is real. Thus the system always supports zero modes for $\lambda^R = 0$.

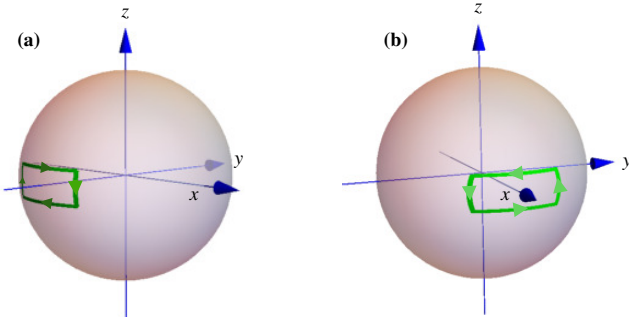


FIG. 9. (Color online) Effective spinor paths followed by the zero modes of H' (Eq. 27) when $\vec{\Delta}(x)$ rotates between the \hat{z} and \hat{x} directions (Bloch walls). In (a) the DW's point in opposite directions ($p = 1$); in (b) they point in the same direction ($p = -1$).

2. k_x^* and Spinor Precession

It is interesting that with in-plane effective Zeeman fields, the zero modes end up at $k_x^* \neq 0$, which was not the case when the Zeeman field was strictly in the \hat{z} direction. This behavior has an interesting interpretation. The zero modes of H' (Eq. 27) must solve a first-order differential equation, $i\partial_x \vec{\psi} = \frac{\tau_x}{v_F} \Delta(x) \cdot \vec{\sigma} \vec{\psi}$, whose solution is formally equivalent to the evolution of a spinor in a time-dependent magnetic field, if one identifies x as a time coordinate. In our model of piecewise-constant $\vec{\Delta}(x)$, this evolution is a precession of the spinor around the locally constant magnetic field direction, and because of the boundary condition, allowed solutions must corre-

spond to orbits that close on themselves. Fig. 9 qualitatively illustrates such paths for Bloch domain walls, for the cases $p = 1$ (a) and $p = -1$ (b). In both the trajectories are formed by alternating rotations around the \hat{z} and \hat{x} directions, but in the $p = -1$ case the \hat{x} rotations have the same sense while in the $p = 1$ case they have opposite senses. Because these loops enclose non-vanishing areas, the wavefunctions pick up a non-trivial phases in going from $x = 0$ to $x = L$, so that the solutions have $k_x^* \neq 0$. This is in contrast to what must happen when $\vec{\Delta}(x)$ is along the \hat{z} direction throughout its evolution, in which case the trajectory is a single line segment along which the trajectory rocks back and forth. This has vanishing enclosed area so that $k_x^* = 0$, consistent with what we found for the zero modes in the last section. Thus the value of k_x^* at which the zero modes appear are a direct measure of the non-trivial phase accumulated when a spin degree of freedom traverses an open loop.

Three comments are in order. Firstly, for each of the loops shown in Fig. 9, there is a second solution orbiting the same axis but on the other side of the sphere. These solutions accumulate the opposite phase of the ones shown, so that one finds solutions at both k_x^* and $-k_x^*$. Second, because the solutions shown are for fixed $\tau_x = \pm 1$, for each of k_x^* and $-k_x^*$ there are two degenerate solutions. Finally, it must be emphasized that the fact that these are zero modes does not dictate that they are Dirac points. We shall see below that they are for $p = 1$, but for $p = -1$, they are individual points along zero energy contours in the (k_x, k_y) plane. However, for $\lambda^R > 0$ the latter surfaces become gapped, except for two Dirac points.

3. Perturbative Treatment of SOC

SOC admixes the zero energy modes, with different possible effects, which we evaluate within perturbation theory. To do so, we write the Hamiltonian in the vicinity of $\vec{k} = (k_x^*, 0) \equiv \vec{k}^*$ as

$$H_{\vec{k}^*} = v_F(\vec{k}^* + \vec{q}) \cdot \vec{\tau} + \vec{\Delta}(x) \cdot \vec{\sigma} + \frac{\lambda^R}{2} (\sigma_x \tau_y - \sigma_y \tau_x). \quad (35)$$

By construction we have two zero energy states at \vec{k}^* for $\lambda^R = 0$, one for each value of τ_x , which we write as kets in the form $|\tau_x\rangle$, where it is implicit that these two states correspond to a specific choice of \vec{k}^* . Projecting Eq. 35 into this subspace, one obtains

$$\bar{H}_{\vec{k}^*} = \begin{pmatrix} v_F q_x - \frac{\lambda^R}{2} \langle 1 | \sigma_y | 1 \rangle & i v_F q_y \langle 1 | \tau_y | -1 \rangle + i \frac{\lambda^R}{2} \langle 1 | \sigma_x \tau_y | -1 \rangle \\ -i v_F q_y \langle -1 | \tau_y | 1 \rangle - i \frac{\lambda^R}{2} \langle -1 | \sigma_x \tau_y | 1 \rangle & -v_F q_x + \frac{\lambda^R}{2} \langle -1 | \sigma_y | -1 \rangle \end{pmatrix}, \quad (36)$$

with energy spectrum

$$\varepsilon(\vec{q}) = \frac{\lambda^R}{4} \left(-\langle 1|\sigma_y|1\rangle + \langle -1|\sigma_y|-1\rangle \right) \pm \left\{ \left[v_F q_x - \frac{\lambda^R}{4} \langle 1|\sigma_y|1\rangle + \frac{\lambda^R}{4} \langle -1|\sigma_y|-1\rangle \right]^2 + \left| v_F q_y \langle -1|\tau_y|1\rangle + \frac{\lambda^R}{2} \langle -1|\sigma_x\tau_y|1\rangle \right|^2 \right\}^{1/2}. \quad (37)$$

The qualitative effect of SOC on the Dirac points thus depends on just a few matrix elements. If $\langle 1|\sigma_y|1\rangle - \langle -1|\sigma_y|-1\rangle \neq 0$, they are shifted away from zero energy. For $\langle 1|\sigma_y|1\rangle + \langle -1|\sigma_y|-1\rangle \neq 0$, their position along the k_x axis is changed, while $\text{Re}(\langle -1|\sigma_x\tau_y|1\rangle / \langle -1|\tau_y|1\rangle) \neq 0$ shifts them off the k_x axis onto a finite k_y^* . Finally $\text{Im}(\langle -1|\sigma_x\tau_y|1\rangle / \langle -1|\tau_y|1\rangle) \neq 0$ opens a gap in the spectrum.

What one needs to know about these various matrix elements can be determined with the help of Fig. 8 and by noting that for $\lambda^R = 0$ the Hamiltonian has chiral operators for the Néel and Bloch wall cases. For the former case, $\chi_N \equiv \sigma_x\tau_z$ obeys $\{H', \chi_N\} = 0$, whereas in the latter, $\chi_B \equiv \sigma_y\tau_z$ obeys $\{H', \chi_B\} = 0$. This means (for the appropriate case) we can relate the basis states by $|s\rangle = \chi_{N,B}|-s\rangle$, with $s = \pm 1$. Note these choices of chiral operators preserve the property $\tau_x|s\rangle = s|s\rangle$. There are four situations to consider:

(i) *Bloch walls*, $p = 1$ – In this case the Bloch walls are oppositely oriented. As illustrated in Fig. 9(a), the wavefunction describes a trajectory that symmetrically encloses \hat{y} axis in the spin-space, so for example $\langle 1|\sigma_y|1\rangle \neq 0$. Using $\chi_B|1\rangle = |-1\rangle$, $[\chi_B, \sigma_y] = 0$, and $\chi_B^2 = 1$, we see $\sum_s \langle s|\sigma_y|s\rangle \neq 0$, and $\sum_s s \langle s|\sigma_y|s\rangle = 0$. We also have

$$\begin{aligned} \langle -1|\sigma_x\tau_y|1\rangle &= \langle 1|\sigma_y\tau_z\sigma_x\tau_y|1\rangle \\ &= \langle 1|\sigma_z\tau_x|1\rangle \\ &= \langle 1|\sigma_z|1\rangle = 0. \end{aligned}$$

The last equality follows from the symmetry of the spinor orbit across the $\hat{x} - \hat{y}$ plane in Fig. 9 (a). The net effect is that the Dirac points are shifted along the k_x axis, but the spectrum is qualitatively the same as in the absence of SOC.

(ii) *Bloch walls*, $p = -1$ – Here the Bloch walls have the same orientation. As in the previous case, $\langle -1|\sigma_x\tau_y|1\rangle = 0$, but now the trajectories encircle the \hat{x} axis [Fig. 9(b)], so that $\langle \pm 1|\sigma_y|\pm 1\rangle = 0$. The SOC has no qualitative effect on the result and we again find zero energy states on the k_x axis. We will verify numerically that these are in fact Dirac points.

(iii) *Néel walls*, $p = 1$ – The σ_y fields are oppositely oriented here. In this case the spin trajectories surround the \hat{x} axis, so $\langle s|\sigma_y|s\rangle = 0$. We also have

$$\begin{aligned} \langle -1|\sigma_x\tau_y|1\rangle &= \langle 1|\sigma_x\tau_z\sigma_x\tau_y|1\rangle \\ &= -i\langle 1|\tau_x|1\rangle = -i \end{aligned}$$

and

$$\begin{aligned} \langle -1|\tau_y|1\rangle &= \langle 1|\sigma_x\tau_z\tau_y|1\rangle \\ &= -i\langle 1|\sigma_x|1\rangle, \end{aligned}$$

which is also pure imaginary. In this case the Dirac point is shifted to a non-vanishing value of k_y^* .

(iv) *Néel walls*, $p = -1$ – This realization has a net σ_y within a unit cell because the DW's have the same orientation. The spin trajectories surround the \hat{y} axis, and $\langle s|\sigma_y|s\rangle = -\langle -s|\sigma_y|-s\rangle$. The results $\langle -1|\sigma_x\tau_y|1\rangle = -i$ and $\langle -1|\tau_y|1\rangle = -i\langle 1|\sigma_x|1\rangle$ are unchanged from case (iii) above; however, here $\langle 1|\sigma_x|1\rangle = 0$. The two eigenvalues of Eq. 36 are then

$$\varepsilon(\vec{q}) = \frac{\lambda^R}{2} \langle 1|\sigma_y|1\rangle \pm \sqrt{\left(\frac{\lambda^R}{2}\right)^2 + v_F^2 q_x^2}. \quad (38)$$

Along the k_x axis a gap has opened up, but with the two energy eigenvalues no longer equal and opposite. However, the opening of a gap at this point does not imply that the system has become insulating. We address what actually happens next using numerical solutions of the tight-binding model.

D. Tight-Binding Results

We have performed tight-binding calculations for the configurations shown in Fig 8. For domain walls with in-plane fields in opposite directions ($p=+1$), the results are similar to those obtained with an uniformly rotating exchange field (Fig.7) and are in agreement with the discussion above: for $\lambda^R = 0$ one finds Dirac points on the k_x axis, which for small λ^R remain there in the Bloch wall case, and are shifted onto the $k_x - k_y$ plane in the Néel wall case. For $p = -1$ – in-plane fields in the same direction – one obtains very different results even for $\lambda^R = 0$. This is illustrated in Fig. 10(a), which shows the surface $\epsilon(\vec{k}) = 0$ forms a closed loop around the K point. The valence and conduction bands actually cross along this loop, so that the system is a metal, and all the states on this constant energy surface are doubly degenerate. Note that the picture is identical for both Bloch and Néel walls because without SOC, the two structures are related by spin-rotational symmetry.

When SOC is added, the two degenerate states along the loops repel, except at individual points, changing the system into a Dirac semimetal. For the Bloch case the resulting Dirac points are on the k_x axis, in agreement with case (ii) above. This is illustrated in Fig. 10(b). In

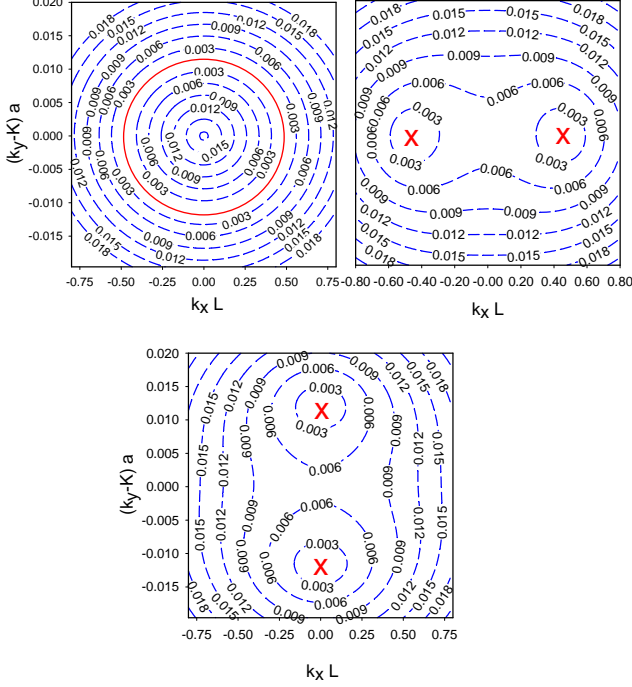


FIG. 10. (Color online) Contour plots of the energy gap obtained by diagonalizing the tight-binding Hamiltonian in presence of a piecewise constant rotating Zeeman field with $p=-1$, see Fig 8. The calculations use $\Delta_0=0.02t$ and $L=43.3a$. In the numerical calculation the four regions appearing in Fig. 8 all have the same width. In (a), the Rashba spin orbit coupling is zero and the system is metallic with a Fermi loop marked in red in the contour plot. For finite Rashba coupling the system becomes a semimetal. In (b) and (c) we show constant energy contour plots for Bloch and Néel domain walls respectively, in both cases with $\lambda_R=0.03t$. In (b) and (c) the red crosses indicate the position of the Dirac points.

the Néel case, there are no zero energy states on the k_x axis, and the positive and negative energy states appear asymmetrically around $\epsilon = 0$, again in agreement with the analysis above [case (iv)]. However, there are nevertheless Dirac points on the k_y axis, as illustrated in Fig. 10(c). Clearly these are not captured by the perturbative analysis above.

Finally it is interesting to compare and contrast the results for $p = -1$ DW's with those of uniform Zeeman fields in the \hat{x} and \hat{y} directions discussed in Section III A above. In the latter case (Néel walls) the results are quite similar to simply applying a uniform field in the \hat{y} direction coupling to the spin, for which one finds Dirac points on the k_y axis. In the former (Bloch wall) case, however, whereas the uniform field resulted in metallic behavior – zero energy states forming finite size loops in momentum space – when the in-plane field is made periodic, the states admix and repel, except at the two points on the k_x axis, turning the system into a Dirac semimetal.

IV. SUMMARY AND CONCLUSION

In this study we have demonstrated that graphene with induced spin-orbit coupling and a periodic Zeeman field supports a remarkably rich set of possible behaviors near zero energy. Depending on how the Zeeman field is arranged, one may obtain a metal, an insulator, or (in most cases) a Dirac semimetal. The positions of the Dirac points in this last case may be adjusted by varying the relative strengths of SOC (λ^R) and the periodic Zeeman field ($\vec{\Delta}(x)$), or the precise way in which $\vec{\Delta}(x)$ varies in the unit cell. Unlike the case of $\lambda^R = 0$, the K and K' points are always gapped when there is SOC.

We find that when $\vec{\Delta}(x) \parallel \hat{z}$ everywhere in the unit cell, the Dirac points are always on the k_y axis, and in most cases there are four of these, two each on either side of the K and K' points. While for $\lambda^R = 0$ there are higher order Dirac points along the same direction in momentum space, these are usually eliminated by SOC, although for narrow ranges of parameters there can be more Dirac points. When the possibility of in-plane fields due to a rotating $\vec{\Delta}(x)$ is allowed, we find the system is generically a Dirac semimetal, although the positions of the Dirac points in the Brillouin zone are sensitive to the details of how such rotations are realized.

Certainly the simplest way to introduce in-plane fields is via a uniform magnetic field imposed in addition to any effective periodic Zeeman field in the system. When the latter is purely in the \hat{z} direction, we found that the system can be made into a metal, a Dirac semimetal, or an insulator, by varying only the direction of the uniform field. In the last case the band structure of the system carries non-trivial topology, and we demonstrated that the system supports a quantized anomalous Hall effect.

It will be interesting to examine transport in this system, to ascertain what signatures the changes in the spectrum as $\vec{\Delta}(x)$ is varied may present in such experiments. Another interesting related direction would be to examine whether such physics occurs on the surfaces of topological insulators, or in thin film topological insulators, where SOC is intrinsic and one need not induce it artificially as in graphene. Finally, the question of how imperfectly formed superlattices behave in terms of their spectra and transport will be particularly relevant to any experiments on systems such as what we have studied in this work. We leave these as problems for future research.

V. APPENDIX: ZERO MODES ON k_y AXIS: Δ_z MODEL

In this appendix, we describe a transfer matrix analysis through which one may identify zero modes as a function of k_x, k_y for this system, and show specifically that in the absence of in-plane Zeeman fields such modes are generically present. The calculation is considerably more

involved than the perturbative analysis described in the main text, but demonstrates that the basic observation – the presence of (gapless) Dirac points on the k_y axis when both a periodic Zeeman field in the \hat{z} direction and Rashba spin-orbit coupling are present – is valid to all orders in perturbation theory.

We begin by reiterating the Hamiltonian of the system,

$$H = v_F(p_x\tau_x + p_y\tau_y) + \Delta_z(x)\sigma_z + \frac{\lambda^R}{2}(\sigma_x\tau_y - \sigma_y\tau_x), \quad (39)$$

where it is assumed that $\Delta_z(-x) = -\Delta_z(x)$. For simplicity we consider piecewise constant forms for $\Delta_z(x)$, and we are interested in spatially periodic realizations, $\Delta_z(x+L) = \Delta_z(x)$. To solve for zero modes one needs to find solutions to $H\vec{\Phi}(x) = 0$ that are Bloch functions, which have the form

$$\vec{\Phi}(x) = \vec{\psi}(x)e^{iQ(x)x + ik_y y}$$

with $\vec{\psi}(x)$ and $Q(x)$ piecewise constant.

A. Zero Modes in Regions of Constant Δ_z

Within the regions of constant Δ_z , $\vec{\psi}(x)$ satisfies $H_Q\vec{\psi} = 0$, with

$$H_Q = v_F[Q\tau_x + k_y\tau_y] + \Delta_z\sigma_z + \frac{\lambda^R}{2}(\sigma_x\tau_y - \sigma_y\tau_x).$$

Note that Q may be complex, so that H_Q is not generally Hermitian. Solving this equation may be simplified by noticing that H_Q has a chiral operator χ_Q (i.e., $\{\chi_Q, H_Q\} = 0$), given by

$$\chi_Q = (Q\tau_y - k_y\tau_x)(Q\sigma_y - k_y\sigma_x).$$

The operator χ_Q is easily diagonalized and has two eigenvalues,

$$\pm K^2 \equiv \pm(Q^2 + k_y^2),$$

and because H_Q anticommutes with χ_Q , one knows that an eigenvector of χ_Q in the $\pm K^2$ sector must either be mapped to the $\mp K^2$ sector by H_Q , or annihilated by it. Eigenvectors of χ_Q may be written in terms of the eigenvectors of $Q\mu_y - k_y\mu_x$, where $\mu_{x,y,z}$ are generic Pauli matrices [i.e., acting either on sublattice ($\vec{\tau}$) or spin ($\vec{\sigma}$)], which satisfy

$$(Q\mu_y - k_y\mu_x) \frac{1}{\mathcal{N}} \begin{pmatrix} -iQ - k_y \\ \pm K \end{pmatrix} = \pm K \frac{1}{\mathcal{N}} \begin{pmatrix} -iQ - k_y \\ \pm K \end{pmatrix},$$

where $\mathcal{N} = [|K|^2 + |iQ + k_y|^2]^{1/2}$. The kets $|\pm, Q\rangle_\mu$ represent eigenvectors corresponding to eigenvalues $\pm K$. Eigenvectors of χ_Q with eigenvalue K^2 are then $|+, Q\rangle_\tau |+, Q\rangle_\sigma$ and $|-, Q\rangle_\tau |-, Q\rangle_\sigma$, and those with eigenvalue $-K^2$ are $|+, Q\rangle_\tau |-, Q\rangle_\sigma$ and $|-, Q\rangle_\tau |+, Q\rangle_\sigma$. Writing $|\pm, Q\rangle_\tau |\pm, Q\rangle_\sigma \equiv |\pm, \pm; Q\rangle$, one finds

$$\begin{aligned} H_Q|++; Q\rangle &= \left(\Delta_z + i\frac{\lambda^R}{2}\right)|+-; Q\rangle + \left(iv_F K - i\frac{\lambda^R}{2}\right)|-+; Q\rangle, \\ H_Q|--; Q\rangle &= \left(-iv_F K - i\frac{\lambda^R}{2}\right)|+-; Q\rangle + \left(\Delta_z + i\frac{\lambda^R}{2}\right)|-+; Q\rangle, \\ H_Q|+-; Q\rangle &= \left(\Delta_z - i\frac{\lambda^R}{2}\right)|++; Q\rangle + \left(iv_F K + i\frac{\lambda^R}{2}\right)|--; Q\rangle, \\ H_Q|-+; Q\rangle &= \left(-iv_F K + i\frac{\lambda^R}{2}\right)|++; Q\rangle + \left(\Delta_z - i\frac{\lambda^R}{2}\right)|--; Q\rangle. \end{aligned} \quad (40)$$

As expected H_Q maps chiral states across sectors.

We can now search for zero energy states within a particular sector. For example, writing

$$|\psi_+[Q]\rangle = a|++; Q\rangle + b|--; Q\rangle,$$

using Eqs. 40 one finds H_Q annihilates this state if

$$\begin{pmatrix} \Delta_z + i\frac{\lambda^R}{2} & -iv_F K - i\frac{\lambda^R}{2} \\ iv_F K - i\frac{\lambda^R}{2} & \Delta_z + i\frac{\lambda^R}{2} \end{pmatrix} \begin{pmatrix} a \\ b \end{pmatrix} = 0. \quad (41)$$

Non-trivial solutions of Eq. 41 exist when $(v_F K)^2 = \Delta_z^2 + i\lambda^R \Delta_z$, or, alternatively,

$$v_F Q = \pm [-v_F^2 k_y^2 + \Delta_z^2 + i\lambda^R \Delta_z]^{1/2} \equiv \pm v_F \tilde{Q}.$$

With this technique, we can generate four zero energy states in a region of constant Δ_z :

$$\begin{aligned} |\psi_+[\tilde{Q}]\rangle &\equiv a|++;\tilde{Q}\rangle + b|--;\tilde{Q}\rangle, \\ |\psi_+[-\tilde{Q}]\rangle &\equiv a|++;-\tilde{Q}\rangle + b|--;-\tilde{Q}\rangle, \\ |\psi_-[\tilde{Q}^*]\rangle &\equiv a^*|+-;\tilde{Q}^*\rangle + b^*|+-;\tilde{Q}^*\rangle, \\ |\psi_-[-\tilde{Q}^*]\rangle &\equiv a^*|+-;-\tilde{Q}^*\rangle + b^*|+-;-\tilde{Q}^*\rangle, \end{aligned} \quad (42)$$

with $a = iv_F K + i\lambda^R/2$, $b = \Delta_z + i\lambda^R/2$, and $v_F K = \sqrt{\Delta_z^2 + i\lambda^R \Delta_z}$.

B. Generalized Mirror Symmetry

We next need to match the solutions in Eqs. 42 corresponding to $\Delta_z > 0$, which we can assume for concreteness to be in the region $0 < x < L/2$, to those corresponding to $\Delta_z < 0$ in the interval $-L/2 < x < 0$. To do so we define x -dependent wavefunctions via $\vec{\Psi} = \vec{\psi}(x)e^{iQ(x)x}$,

which for zero modes obeys the equation $H_{k_y}\vec{\Psi} = 0$, with

$$H_{k_y} = v_F[(-i\partial_x)\tau_x + k_y\tau_y] + \Delta_z(x)\sigma_z + \frac{\lambda^R}{2}(\sigma_x\tau_y - \sigma_y\tau_x).$$

The matching is simplified by noting that, due to the antisymmetry of $\Delta_z(x)$, H_{k_y} commutes with the generalized mirror operation $X \equiv \tau_y\sigma_x I_x$, where I_x carries out the spatial mirror inversion, $I_x f(x) \equiv f(-x)$ for any $f(x)$. Since $X^2 = 1$, this means we can classify the zero modes into two groups, satisfying $X\vec{\Psi}_\pm = \pm\vec{\Psi}$. The operation is particularly interesting at $x = 0$, where $X\vec{\Psi}_\pm(x = 0) = \tau_y\sigma_x\vec{\Psi}_\pm(x = 0) \equiv \mathcal{M}_y\vec{\Psi}_\pm(x = 0)$, so that at the origin $\vec{\Psi}$ is an eigenstate of the (purely matrix) operation \mathcal{M}_y . In terms of eigenstates of τ_z and σ_z , $|s_1, s_2\rangle_0$, where $\tau_z|s_1, s_2\rangle_0 = s_1|s_1, s_2\rangle_0$ and $\sigma_z|s_1, s_2\rangle_0 = s_2|s_1, s_2\rangle_0$, with $s_1, s_2 = \pm 1$, the action of \mathcal{M}_y is

$$\begin{aligned} \mathcal{M}_y|1, 1\rangle_0 &= i|-1, -1\rangle_0, \quad \mathcal{M}_y|-1, -1\rangle_0 = -i|1, 1\rangle_0, \\ \mathcal{M}_y|1, -1\rangle_0 &= i|-1, 1\rangle_0, \quad \mathcal{M}_y|-1, 1\rangle_0 = -i|1, -1\rangle_0, \end{aligned}$$

which is the action of a Pauli σ_y matrix in each of the two-dimensional sectors defined by $s_1 s_2 = 1$ and $s_1 s_2 = -1$. If one orders the basis states as

$$(|1, 1\rangle, |1, -1\rangle, |-1, 1\rangle, |-1, -1\rangle),$$

the coefficients for the states corresponding to those in Eq. 42 are

$$\vec{\psi}_+[\pm\tilde{Q}] = \begin{pmatrix} (a+b)(\mp i\tilde{Q} - k_y)^2 \\ (a-b)(\mp i\tilde{Q} - k_y)K \\ (a-b)(\mp i\tilde{Q} - k_y)K \\ (a+b)K^2 \end{pmatrix}, \quad \vec{\psi}_-[\pm\tilde{Q}^*] = \begin{pmatrix} (a^*+b^*)(\mp i\tilde{Q}^* - k_y)^2 \\ (a^*-b^*)(\mp i\tilde{Q}^* - k_y)K^* \\ -(a^*-b^*)(\mp i\tilde{Q}^* - k_y)K^* \\ -(a^*+b^*)K^{*2} \end{pmatrix}. \quad (43)$$

With some tedious (albeit straightforward) algebra, we can construct from these eigenstates of \mathcal{M}_y with eigenvalues $m_y = \pm 1$. For $m_y = 1$ one finds

$$\begin{aligned} \vec{\psi}_1[m_y = 1] &= -\left(\frac{1-i}{\sqrt{2}}\right)\left(\frac{i\tilde{Q} - k_y}{4i\tilde{Q}K^2(a+b)}\right)\vec{\psi}_+[\tilde{Q}] + \left(\frac{1-i}{\sqrt{2}}\right)\left(\frac{-i\tilde{Q} - k_y}{4i\tilde{Q}K^2(a+b)}\right)\vec{\psi}_+[-\tilde{Q}] \\ &\quad -\left(\frac{1+i}{\sqrt{2}}\right)\left(\frac{i\tilde{Q}^* - k_y}{4i\tilde{Q}^*K^{*2}(a^*+b^*)}\right)\vec{\psi}_-[\tilde{Q}^*] + \left(\frac{1+i}{\sqrt{2}}\right)\left(\frac{-i\tilde{Q}^* - k_y}{4i\tilde{Q}^*K^{*2}(a^*+b^*)}\right)\vec{\psi}_-[-\tilde{Q}^*], \end{aligned} \quad (44)$$

$$\begin{aligned}
\vec{\psi}_2[m_y = 1] = & \frac{1}{\sqrt{2}} \left[\left(\frac{1+i}{2} \right) \frac{1}{2(a-b)K^3} + \left(\frac{-1+i}{2} \right) \frac{2k_y(a^*+b^*)}{4i\tilde{Q}(a+b)(a^*-b^*)K^*K^2} \right] (i\tilde{Q} - k_y) \vec{\psi}_+[\tilde{Q}] \\
& + \frac{1}{\sqrt{2}} \left[\left(\frac{1+i}{2} \right) \frac{1}{2(a-b)K^3} - \left(\frac{-1+i}{2} \right) \frac{2k_y(a^*+b^*)}{4i\tilde{Q}(a+b)(a^*-b^*)K^*K^2} \right] (-i\tilde{Q} - k_y) \vec{\psi}_+[-\tilde{Q}] \\
& + \frac{1}{\sqrt{2}} \left[\left(\frac{1+i}{2} \right) \frac{-2k_y(a+b)}{4i\tilde{Q}^*(a^*+b^*)(a-b)KK^{*2}} - \left(\frac{-1+i}{2} \right) \frac{1}{2(a^*-b^*)K^{*3}} \right] (i\tilde{Q}^* - k_y) \vec{\psi}_-[\tilde{Q}^*] \\
& + \frac{1}{\sqrt{2}} \left[- \left(\frac{1+i}{2} \right) \frac{-2k_y(a+b)}{4i\tilde{Q}^*(a^*+b^*)(a-b)KK^{*2}} - \left(\frac{-1+i}{2} \right) \frac{1}{2(a^*-b^*)K^{*3}} \right] (-i\tilde{Q}^* - k_y) \vec{\psi}_-[-\tilde{Q}^*].
\end{aligned} \tag{45}$$

States with $m_y = -1$ may be obtained from this by defining an operator \mathcal{M}_x such that $\mathcal{M}_x|s_1, s_2\rangle = |-s_1, -s_2\rangle$, which anticommutes with \mathcal{M}_y , so that $|\psi_i[m_y = -1]\rangle \equiv \mathcal{M}_x|\psi_i[m_y = 1]\rangle$.

C. Wavefunctions for $x \neq 0$ and Wavefunction Matching

In this subsection we describe how one finds values of k_y for which appropriately continuous wavefunctions

with zero energy can be constructed. In particular we do so for $m_y = 1$; The zero modes for $m_y = -1$ can be constructed from these, and in particular will exist at the same values of k_y , as we explain momentarily. Eqs. 44 and 45 represent explicit wavefunctions at $x = 0$, which can be extended into $x > 0$ simply by multiplying each term by the appropriate plane wave. Defining coefficients A_i by writing

$$\vec{\psi}_i[m_y = 1] \equiv A_i[\tilde{Q}]\vec{\psi}_+[\tilde{Q}] + A_i[-\tilde{Q}]\vec{\psi}_+[-\tilde{Q}] + A_i^*[-\tilde{Q}]\vec{\psi}_-[\tilde{Q}^*] + A_i^*[\tilde{Q}]\vec{\psi}_-[-\tilde{Q}^*], \tag{46}$$

one obtains

$$\vec{\Psi}_i[m_y = 1; x] = A_i[\tilde{Q}]e^{iQx}\vec{\psi}_+[\tilde{Q}] + A_i[-\tilde{Q}]e^{-iQx}\vec{\psi}_+[-\tilde{Q}] + A_i^*[-\tilde{Q}]e^{iQ^*x}\vec{\psi}_-[\tilde{Q}^*] + A_i^*[\tilde{Q}]e^{-iQ^*x}\vec{\psi}_-[-\tilde{Q}^*]. \tag{47}$$

For $x < 0$ the wavefunction is obtained using

$$\begin{aligned}
|\Psi_i[m_y; -x]\rangle &= I_x|\Psi_i[m_y; x]\rangle \\
&= \mathcal{M}_y M |\Psi_i[m_y; x]\rangle \\
&= m_y \mathcal{M}_y |\Psi_i[m_y; x]\rangle.
\end{aligned}$$

Note that for general values of x , $|\Psi_i[m_y; x]\rangle$ is *not* an eigenstate of the \mathcal{M}_y operator. However, at two points it is: $x = 0$, where the wavefunction must be continuous [$I_x\vec{\Psi}(x = 0^+) = \vec{\Psi}(x = 0^-)$], and at $x = \pm L/2$, where

$I_x\vec{\Psi}(x = L/2) = \vec{\Psi}(x = -L/2) = e^{ik_x L}\vec{\Psi}(x = L/2)$ due to Bloch's theorem. For the present purpose we focus on states with $k_x = 0$, anticipating from our numerical investigations that Dirac points if present are on the k_y axis when there are no in-plane Zeeman fields. We thus require that eigenstates of the Hamiltonian which are properly continuous are also eigenstates of \mathcal{M}_y at $x = L/2$:

$$\mathcal{M}_y|\Psi[m_y = 1; L/2]\rangle = |\Psi[m_y = 1; L/2]\rangle, \tag{48}$$

where

$$|\Psi[m_y = 1; L/2]\rangle = \sum_{i=1,2} u_i |\Psi_i[m_y = 1; L/2]\rangle \equiv \sum_{i=1,2} u_i \psi_i[s_1, s_2]|s_1, s_2\rangle_0$$

for some coefficients u_i . Note the simplification that different values of m_y are not admixed by the matching conditions.

Equating the coefficients of the various $|s_1, s_2\rangle_0$ states on either side of Eq. 48 generates four equations, although

one quickly recognizes that only two of these are linearly independent. Eq. 48 can thus be satisfied if we can find

coefficients u_1, u_2 such that

$$\begin{pmatrix} \psi_1[1, 1] + i\psi_1[-1, -1] & \psi_2[1, 1] + i\psi_2[-1, -1] \\ \psi_1[1, -1] + i\psi_1[1, -1] & \psi_2[1, -1] + i\psi_2[-1, 1] \end{pmatrix} \begin{pmatrix} u_1 \\ u_2 \end{pmatrix} \equiv \mathbf{D} \begin{pmatrix} u_1 \\ u_2 \end{pmatrix} = 0. \quad (49)$$

The coefficients $\psi_i[s_1, s_2]$ may be obtained explicitly using Eqs. 44, 45, and 46; the expressions are lengthy and not particularly illuminating, and so are not provided here. We note, however, that their forms turn out to guarantee that the matrix \mathbf{D} appearing in Eq. 49 is purely real. Finally, non-trivial solutions to Eq. 49 can be found when

$$D(k_y) \equiv \det \mathbf{D} = 0.$$

The determinant $D(k_y)$ is plotted for various choices of parameters in the main text.

Finally, we come back to the fact that our construction was carried out specifically for $m_y = 1$. Defining $T_{L/2}$ as a translation operator by half a unit cell ($T_{L/2}f(x) = f(x + L/2)$), it is not difficult to show the $[T_{L/2}, I_x] = 0$ within the subspace of functions that are periodic ($f(x + L) = f(x)$). So within our restriction to Bloch states with $k_x = 0$, we can consider the action of the

operator $S \equiv \mathcal{K}T_{L/2}$, where \mathcal{K} denotes complex conjugation. Given a state $\tilde{\Psi}[m_y; x]$ for which $H_{k_y}\tilde{\Psi}[m_y; x] = 0$, it is easy to show that $H_{k_y}S\tilde{\Psi}[m_y; x] = 0$. Moreover, $XS\tilde{\Psi}[m_y; x] = -m_yS\tilde{\Psi}[m_y; x]$, so $S\tilde{\Psi}[m_y; x]$ lies in the opposite subspace from $\tilde{\Psi}[m_y; x]$ under X . Thus we find zero energy states occurring in pairs with different X eigenvalues, and understand that the Hamiltonian does not cause level repulsion between them because $[H_{k_y}, X] = 0$.

ACKNOWLEDGMENTS

This work has been supported by MEyC-Spain under grant FIS2015-64654-P, by Brazilian funding agency Capes, by the NSF through Grant Nos. DMR-1506263 and DMR-1506460, and by the US-Israel Binational Science Foundation.

-
- [1] P. Avouris, Z. Chen, and V. Perebeinos, *Nat Nano* **2**, 605 (2007).
 - [2] K. S. Novoselov, V. I. Fal'ko, L. Colombo, P. R. Gellert, M. G. Schwab, and K. Kim, *Nature* **490**, 192 (2012).
 - [3] A. H. Castro Neto, F. Guinea, N. M. R. Peres, K. S. Novoselov, and A. K. Geim, *Rev. Mod. Phys.* **81**, 109 (2009).
 - [4] M.I.Katsnelson, *Graphene* (Cambridge, 2012).
 - [5] M. Z. Hasan and C. L. Kane, *Rev. Mod. Phys.* **82**, 3045 (2010).
 - [6] X.-L. Qi and S.-C. Zhang, *Rev. Mod. Phys.* **83**, 1057 (2011).
 - [7] D. Xiao, M.-C. Chang, and Q. Niu, *Reviews of Modern Physics* **82**, 1959 (2010).
 - [8] R. V. Gorbachev, J. C. W. Song, G. L. Yu, A. V. Kretinin, F. Withers, Y. Cao, A. Mishchenko, I. V. Grigorieva, K. S. Novoselov, L. S. Levitov, and A. K. Geim, *Science* **346**, 448 (2014).
 - [9] P. San-Jose, A. Gutiérrez-Rubio, M. Sturla, and F. Guinea, *Physical Review B* **90**, 115152 (2014).
 - [10] J. C. W. Song, P. Samutpraphoot, and L. S. Levitov, *Proceedings of the National Academy of Sciences* **112**, 10879 (2015).
 - [11] Z. Qiao, S. A. Yang, W. Feng, W.-K. Tse, J. Ding, Y. Yao, J. Wang, and Q. Niu, *Phys. Rev. B* **82**, 161414 (2010).
 - [12] Z. Qiao, H. Jiang, X. Li, Y. Yao, and Q. Niu, *Physical Review B* **85**, 115439 (2012).
 - [13] H. Zhang, C. Lazo, S. Blügel, S. Heinze, and Y. Mokrousov, *Physical Review Letters* **108**, 056802 (2012).
 - [14] W.-K. Tse, Z. Qiao, Y. Yao, A. H. MacDonald, and Q. Niu, *Phys. Rev. B* **83**, 155447 (2011).
 - [15] Z. Qiao, X. Li, W.-K. Tse, H. Jiang, Y. Yao, and Q. Niu, *Physical Review B* **87**, 125405 (2013).
 - [16] L. Brey, *Physical Review B* **92**, 235444 (2015).
 - [17] Z. Qiao, W. Ren, H. Chen, L. Bellaiche, Z. Zhang, A. H. MacDonald, and Q. Niu, *Physical Review Letters* **112**, 116404 (2014).
 - [18] L. Brey and H. A. Fertig, *Phys. Rev. Lett.* **103**, 046809 (2009).
 - [19] C.-H. Park, Y.-W. Son, L. Yang, M. L. Cohen, and S. G. Louie, *Physical Review Letters* **103**, 046808 (2009).
 - [20] M. Barbier, P. Vasilopoulos, and F. M. Peeters, *Physical Review B* **81**, 075438 (2010).
 - [21] D. P. Arovas, L. Brey, H. A. Fertig, E.-A. Kim, and K. Ziegler, *New Journal of Physics* **12**, 123020 (2010).
 - [22] P. Burset, A. L. Yeyati, L. Brey, and H. A. Fertig, *Physical Review B* **83**, 195434 (2011).
 - [23] C. Park, L. Yang, Y. Son, M. Cohen, and S. Louie, *Nature Physics* **4**, 213 (2008).
 - [24] D. Huertas-Hernando, F. Guinea, and A. Brataas, *Phys. Rev. B* **74**, 155426 (2006).
 - [25] H. Min, J. E. Hill, N. A. Sinitsyn, B. R. Sahu, L. Kleinman, and A. H. MacDonald, *Phys. Rev. B* **74**, 165310 (2006).

- [26] L. Chico, M. P. López-Sancho, and M. C. Muñoz, Phys. Rev. B **79**, 235423 (2009).
- [27] A. H. Castro Neto and F. Guinea, Phys. Rev. Lett. **103**, 026804 (2009).
- [28] J. Balakrishnan, G. Kok Wai Koon, M. Jaiswal, A. H. Castro Neto, and B. Özyilmaz, Nat Phys **9**, 284 (2013).
- [29] A. T. Costa, M. S. Ferreira, T. Hallam, G. S. Duesberg, and A. H. C. Neto, EPL (Europhysics Letters) **104**, 47001 (2013).
- [30] O. Céspedes, M. S. Ferreira, S. Sanvito, M. Kociak, and J. M. D. Coey, Journal of Physics: Condensed Matter **16**, L155 (2004).
- [31] J. J. Palacios, J. Fernández-Rossier, and L. Brey, Physical Review B **77**, 195428 (2008).
- [32] J. J. Palacios, J. Fernández-Rossier, and L. Brey, Semiconductor Science and Technology **25**, 033003 (2010).
- [33] K. M. McCreary, A. G. Swartz, W. Han, J. Fabian, and R. K. Kawakami, Physical Review Letters **109**, 186604 (2012).
- [34] C. L. Kane and E. J. Mele, Phys. Rev. Lett. **95**, 226801 (2005).
- [35] J. Sun, H. A. Fertig, and L. Brey, Phys. Rev. Lett. **105**, 156801 (2010).
- [36] We assume that the magnitude and period of the exchange field are weak enough so that no new Dirac points are induced in the band structure.
- [37] I. Martin, Y. M. Blanter, and A. F. Morpurgo, Phys. Rev. Lett. **100**, 036804 (2008).
- [38] J. Li, I. Martin, M. Buttiker, and A. F. Morpurgo, Nat Phys **7**, 38 (2011).
- [39] M. Barbier, P. Vasilopoulos, F. M. Peeters, and J. M. Pereira, Physical Review B **79**, 155402 (2009).
- [40] M. Killi, S. Wu, and A. Paramakanti, Physical Review Letters **107**, 086801 (2011).
- [41] L. Z. Tan, C.-H. Park, and S. G. Louie, *Nano Letters*, **11**, 2596 (2011).